

Full length article

## Track geometry prediction for Laser Metal Deposition based on on-line artificial vision and deep neural networks

Martina Perani <sup>a</sup>, Stefano Baraldo <sup>b,\*</sup>, Michael Decker <sup>a</sup>, Ambra Vandone <sup>b</sup>, Anna Valente <sup>b</sup>, Beatrice Paoli <sup>a</sup>

<sup>a</sup> Laboratory for Web Science, Fernfachhochschule Schweiz (FFHS), Brig, Switzerland

<sup>b</sup> Department of Innovative Technologies, University of Applied Science and Arts of Southern Switzerland (SUPSI), Lugano, Switzerland

### ARTICLE INFO

#### Keywords:

Additive manufacturing  
Artificial intelligence  
Convolutional neural networks  
Laser Metal Deposition  
Machine learning  
Process quality

### ABSTRACT

Laser Metal Deposition (LMD) is an additive manufacturing technology that attracts great interest from the industry, thanks to its potential to realize parts with complex geometries in one piece, and to repair damaged ones, while maintaining good mechanical properties. Nevertheless, the complexity of this process has limited its widespread adoption, since different part geometries, strategies and boundary conditions can yield very different results in terms of external shapes and inner flaws. Moreover, monitoring part quality during the process execution is very challenging, as direct measurements of both structural and geometrical properties are mostly impracticable. This work proposes an on-line monitoring and prediction approach for LMD that exploits coaxial melt pool images, together with process input data, to estimate the size of a track deposited by LMD. In particular, a novel deep learning architecture combines the output of a convolutional neural network (that takes melt pool images as inputs) with scalar variables (process and trajectory data). Various network architectures are evaluated, suggesting to use at least three convolutional layers. Furthermore, results imply a certain degree of invariance to the number and size of dense layers. The effectiveness of the proposed method is demonstrated basing on experiments performed on single tracks deposited by LMD using powders of Inconel 718, a relevant material for the aerospace and automotive sectors.

### 1. Introduction

Laser Metal Deposition (LMD) is an additive manufacturing technology where a stream of powder particles is blown out from a set of nozzles (Fig. 1) transported by a carrier gas. The particles intercept a laser beam that provides the necessary energy to fuse them, resulting in the formation of a melt pool, i.e. a drop of molten metal. As the deposition head advances, the nozzle and the laser beam move according to the desired product geometry, the melt pool subsequently cools down and evolves into a solid metal track [1].

When compared with Powder Bed Fusion (PBF), the most consolidated powder-based metal AM technology, LMD has a much greater potential:

- efficient use of powders: in LMD, powder is blown only over the deposition spot, whereas in PBF the whole deposition plate is filled with powder, most of which is not melted;
- use of 5-axis manufacturing strategies, whereas PBF is intrinsically 3-axis-based;

- achievement of greater work volumes, usually limited in PBF below  $250 \times 250 \times 300$  mm;
- possibility of part repairing, i.e. deposition of new, functional material on damaged regions of used products;
- integration on existing machine tools with limited modifications, thus opening the exploitation potential to an extremely large market (tens of thousands of machines, during the next 5 years);

On the other side, LMD does not benefit from the repeatability and the good thermal diffusion properties given by the powder bed; consequently, metal parts formed by this technique may present various defects, such as significant deviations from the reference geometry, low mechanical performances, presence of pores and residual stresses [1]. These poor qualities may arise when producing new, untested geometries and materials for which optimal parameters are unknown, because of the high complexity of this AM process [2]. For these reasons, researchers have been actively developing modeling and control of LMD in recent years, trying to get the most out of such a promising

\* Correspondence to: Dipartimento Tecnologie Innovative (DTI), Scuola universitaria professionale della Svizzera italiana (SUPSI), via La Santa 1, CH-6962, Viganello, Switzerland.

E-mail address: [stefano.baraldo@supsi.ch](mailto:stefano.baraldo@supsi.ch) (S. Baraldo).

<https://doi.org/10.1016/j.rcim.2022.102445>

Received 14 May 2021; Received in revised form 7 July 2022; Accepted 16 August 2022

Available online 5 September 2022

0736-5845/© 2022 The Author(s). Published by Elsevier Ltd. This is an open access article under the CC BY license (<http://creativecommons.org/licenses/by/4.0/>).

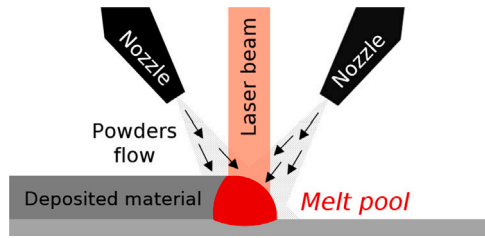


Fig. 1. Sketch of LMD functioning principle.

technology. Accurate multi-physics modeling and simulation of this process is being developed by many research teams, obtaining promising results in recent years [3,4], but achieving meaningful accuracy on very small domains (few  $\text{cm}^2$ ) requires a lot of time (about 1 h per cm of deposition path), thus making this kind of models useful for process engineering but not in the context of process control; moreover, initial and boundary conditions and model parameters, even when carefully evaluated, can never account for the full complexity and stochasticity of some of the involved phenomena, such as particle bumping. For this reason, another branch of literature is dedicated to process monitoring, on-line prediction and real-time control.

This work is focused on this second approach to improving product quality of LMD. First, since the automated labeling of LMD data for machine learning purposes has not been addressed in literature, a pipeline for acquiring inputs and feedbacks during the deposition, and associating them to process outcomes, is proposed. Second, based on the data sets assembled with this approach, the use of a Deep Learning System (DLS) made of Convolutional Neural Networks (CNNs) and a combined fully connected network is proposed, to predict the track geometry starting from both process input parameters (such as power, velocity and powder feeding rate) and melt pool images captured on-line; this architecture, which combines melt pool images and machine command data, has never been proposed before for local estimation of track geometry in LMD. The obtained on-line predictive model is suitable for being used in a closed-loop control method to modulate input parameters, with the aim of tracking the desired track size.

The paper is structured as follows. Section 2 briefly reviews state of the art of LMD process monitoring and prediction. Section 3 presents the experimental setup and the proposed methodologies for data fusion and for training the predictive model. Section 4 presents the performances of the proposed AI model in predicting track size thanks to the exploitation of on-line images. Finally, Section 5 presents some concluding remarks about the presented solution and its future development and applications.

## 2. State of the art

This section summarizes briefly the existing technologies and methods for monitoring LMD and evaluating its outcomes, to motivate the solution chosen for this work. Moreover, the main approaches in the field of machine learning for LMD are reported, to highlight the novelty of the proposed approach with respect to previous efforts found in literature.

### 2.1. LMD monitoring and inspection

#### 2.1.1. Process feedback data

Because of the working principles of LMD, it is quite difficult to integrate direct process outcome measurement devices in an industrial machine; for example, geometry measurement can be effectively performed only at discrete intervals during the process, e.g., after at least one full layer is finished [5,6]. Therefore, when finer deposition monitoring is required, to prevent highly localized defects, most of the

available continuous monitoring solutions that are industrially mature and reliable can provide only indirect process feedbacks.

Dual-color pyrometers [7] can provide direct temperature measurements, after proper calibration, averaged on a measurement spot (e.g. 1 mm diameter), therefore they can provide a high-speed, integral measurement of the melt pool energy content. On the contrary, matrix sensors can provide richer, spatially distributed information, but at the expense of other drawbacks. First, industrial cameras can be heavily affected by phenomena that emit strong light, e.g. sparks or vapor, as they work mostly on visible-light frequencies. Narrow band or NIR filters can be used to mitigate these effects, as proposed for example in [8]. Second, the acquired melt pool intensity is not directly interpretable as a temperature. Finally, the sampling time of an industrial camera can usually reach few hundreds of FPS, well below the high frequencies (up to 100 kHz) of a pyrometer signal. Thermal [9] and hyperspectral [10] cameras can partially solve the shortcomings of visible-light cameras, but they are usually limited in terms of resolution, speed and integrability to be effective in capturing the process dynamics. Another option, still in its infancy, is represented by acoustic sensing [11] for the detection of cracks formation, although retrieving localized information about process status with this kind of technology is still very challenging. An extensive overview about LMD monitoring approaches can be found in [12].

All of these methods offer, to some degree, information about temperature or energy density variations, which are correlated to the resulting mechanical properties of the part [13]. Matrix sensors can provide information also about the geometry of the track in progress, from a 2D perspective, and many studies use them by extracting handcrafted features, like melt pool area, diameter, asymmetry, or other proxy measurements of track shape and energy content [14,15].

Considering cost and ease of integration, beam-coaxial imaging by visible-light cameras remains the most convenient and cost-effective solution, as nearly any deposition head for LMD can be easily equipped with a monitoring camera into the optical chain. For this reason, it was decided to focus on a vision setup that could be implemented on a wide range of existing machines.

#### 2.1.2. Outcome data

Measuring process outcomes is mandatory for assessing the quality of produced parts, but it is also fundamental for training a prediction model. Process outcomes for LMD can be classified as geometric and mechanical. In this work, the focus is set on the prediction of track geometry, which is essential even at layer level to avoid size drifts and therefore large distortions of the final part. Nonetheless, it must be noted that the methodology presented in this work could be extended in the future to correlate on-line feedbacks also with structural properties of a part, although such indices are usually measurable only on coarse spatial grids (e.g., part cuts for assessing porosity can only be performed with few millimeters of distance from each other). Some details about mechanical testing and microstructural measurements for LMD can be found in [13].

Non-destructive measurements, comprehensively reviewed in [16], are usually performed to reconstruct the overall geometry of the manufactured part, for example by means of fringe projection 3D scanning [17] or X-ray Computed Tomography [18]. In particular, [17] identified the former as the ideal solution for metal AM, as the trade-off between speed, field of view, resolution and adaptability to surface properties fits well typical AM parts. For this reason, this technology has been used also in this work to acquire deposition geometries.

### 2.2. Machine learning methods for LMD

The relationships between the properties of AM-deposited parts, the deposition process itself and the deposition parameters are quite complex, therefore achieving an accurate model that describes these inter-relations is of great importance to reliably build AM parts with a desired

geometry. To help overcoming the computational efforts required with multi-physics models, an increasing adoption of Neural Networks (NNs) and Machine Learning (ML) methods in additive manufacturing is observed, which can be categorized into design for AM, in-situ monitoring, and process–property–performance linkage [19]. This work focuses on the latter, where a lot of research is focused on fused deposition modeling [20–22] and selective laser sintering [23–28], whereas few results are reported in the field of laser metal deposition [29].

For laser metal deposition processes, like LMD, research has been done using various different materials, models and aims. In [29], the geometrical accuracy of 2024 Al alloy single tracks is predicted with NNs using laser power, powder supply and deposition speed as inputs. The geometry of the deposited parts was evaluated cutting a cross-section for each deposited track and the height, width and depth of the cross-section were given as target to the neural network, without following the process in its temporal evolution. In [30] thermal images are added to process parameters by stacking a CNN with a standard NN in order to predict the distortion of the deposited parts from the planned geometry, basing on the local thermal history. The approach proposed in [30] is promising, as it accounts for the temporal evolution of the temperature during the deposition, but it is not applicable at the boundary of complex parts and with complex geometries comprising internal cavities. Moreover, it relies on thermal images acquired during the deposition process, limiting the applicability of this approach in a process control setting. In [31] features are extracted from thermal images and subsequently multiple machine learning methods, like K-nearest neighbors, Support-Vector Machines (SVM) and Decision Trees, are applied to predict surface roughness. The employment of NNs in the present work removes the need of feature extraction, a necessary step towards on-line process control. Moreover, using models with a higher degree of complexity like NNs can further improve performance, as NNs applied to AM-related tasks empirically outperform other ML methods like SVM and Random Forests [32].

### 3. Methodology

This section describes first of all the equipment used to perform LMD depositions and to acquire process and outcome data. Secondly, the pipeline set up for performing *data fusion*, i.e. for integrating the heterogeneous available sources of information into a coherent data base, is described, and the selected regressors and response variables of the prediction problem at hand are presented. Finally, the deep-learning architecture designed to solve the target prediction problem is detailed.

#### 3.1. Experimental setup and campaign

The machine used for testing the proposed approach is a 3-axis Prima Power Laserdyne 430, equipped with an Optomec four-nozzle LMD head, an Optomec powder feeder, and a Convergent CF1000 fiber laser source, which delivers a 1079.5 nm wavelength beam with maximum 1050 W power on a spot of 1 mm size. An IDS UI-3070CP-C-HQ2 camera has been mounted onto the deposition head, to acquire a top view of the melt pool area thanks to a dichroic mirror in the optical chain. Additionally, a 850 nm narrow band filter cleans up the radiation from several spurious signals and aberrations, thus improving the signal-to-noise ratio, as reported in [8].

During the deposition process, two types of data are acquired:

- **process inputs:** the X, Y and Z axis positions, commanded power and laser activation status (ON/OFF) can be sampled up to 1 kHz and recorded as a new line into a text log-file, directly by the machine controller;
- **process feedback:** melt pool images are acquired by artificial vision at 200 fps by the beam-coaxial camera and cropped on a region of  $400 \times 400$  pixels that is large enough to contain the full melt pool (Fig. 2).

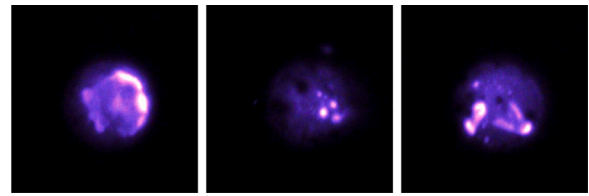


Fig. 2. Melt pool images captured during the initial transient (left), cruise (middle) and final transient (right) of a single track.

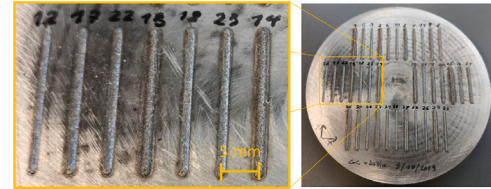


Fig. 3. Inconel 718 substrate with 36 printed tracks.

After the deposition process, the printed sample is dismantled from the machine and moved to a measurement station equipped with a GOM ATOS Core 200 fringe projection scanner. This device produces a 3D mesh with 0.08 mm resolution that represents the built part surface, which allows to measure the desired **process outcomes**: local track width, height and cross-section at every sampled axis position (as described among the process inputs).

The performed experimental campaign is constituted by the deposition of 36 single tracks, printed with nickel alloy Inconel 718 powders ( $77 \pm 30 \mu\text{m}$  diameter), each one of length 20 mm, deposited on a substrate of the same material (10 mm thickness), as shown in Fig. 3, starting from ambient temperature. In particular, fixed parameters were the stand-off distance of 12 mm, the powder flux of 0.032 g/s, the carrier gas flux of 4 l/min and the shielding gas flux of 15 l/min, whereas laser power and speed have been varied on a grid of  $6 \times 6$  values typically used on the test machine, i.e. powers from 200 to 700 W, with step 100 W, and velocities from 300 to 1050 mm/min, with step 150 mm/min (see [33] regarding optimal process windows for LMD). To ensure some degree of independence between tracks, laser powers have been alternated in a high-low sequence, and tracks have been deposited with 3-track spacing.

The resulting sample is analyzed automatically by a pipeline of computer vision techniques, described in detail in Section 3.2, that aligns the traces of process signals with outcome geometries and measures the outcomes considered in this work, i.e. track height, width and cross-section. The integrated data set is then used to train the deep-learning system described in Section 3.3.

#### 3.2. Data fusion

Data collected from the three sources described in Section 3.1, (machine, vision and 3D scanner) must be integrated in a comprehensive data set, to be used as training features and targets, respectively, for the predictive model described in Section 3.3. The integration process, here called *data fusion*, is based on the pipeline outlined in [34], adapted to the experimental infrastructure used in this work and extended to include additional variables. The main steps, with reference to Fig. 4, are described in the following.

All the collected signals must be synchronized to a shared timestamp. This process is carried out by synchronizing both 3D scan and vision data to machine data.

First of all, outcome data must be associated to each point of the process trajectory, since a mesh of the deposited sample obtained by 3D scanning is a purely spatial object, with no reference to the time history

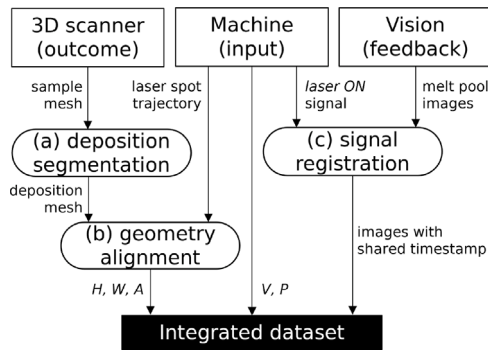


Fig. 4. Diagram of data fusion approach.

of the deposition. To do this, deposition trajectory and sample geometry must be aligned: the latter, as anticipated, is measured outside the LMD machine, therefore the resulting mesh nodes coordinates are expressed in a different reference frame.

Trajectory-to-deposition alignment is performed in two steps:

(a) **Segmentation of deposition and substrate:** a parametric surface is fitted to the substrate of the sample plate, which in our test case is the one shown in the right panel of Fig. 3; since the substrate surface is not perfectly planar, in particular after the thermo-mechanical deformations induced by the LMD process, a low-degree polynomial (e.g. cubic) in  $x$  and  $y$  is usually the best choice to fit the  $z$  coordinate of substrate points. The surface is fitted only to the substrate, and not to mesh vertices corresponding to deposited material, by repeatedly applying the following operations up to convergence:

- fit the polynomial to active mesh vertices with a robust regression method, like the Huber loss function [35];
- exclude vertices whose  $z$  coordinate lies above a small threshold (0.02 mm was ideal in the considered case) from the last fitted polynomial.

At convergence, the set of active points is very similar to the region of substrate that is free from deposition material.

(b) **Alignment of laser spot trajectory with deposition geometry:** laser trajectory points, sampled at 1 ms time step, are aligned to the deposition point cloud, i.e. the complementary of the set of vertices found at the preceding step. This is done in two steps:

- a rough registration, performed by matching the principal axes of inertia of the two point clouds;
- a fine registration, performed by a custom variant of the Iterative Closest Points algorithm [36] that minimizes distances between each trajectory point and the barycenter of deposition vertices found in its neighborhood (the neighborhood radius is set equal to the laser spot radius).

The result of segmentation and alignment operations is illustrated in Fig. 5

When the trajectory-mesh alignment is completed, the mesh can be sectioned at each trajectory point, by a cut plane perpendicular to the laser spot velocity vector. This allows to extract track profiles along all the deposition path, and to perform measurements of the geometrical features that will be used to assess the performances of the DLS described in Section 3.3: **track height  $H$** , **track width  $W$**  and **track cross-section area  $A$** , the desired process outcomes (Fig. 6).

To complete the training data set, also camera images must be referenced to a timestamp that is shared with machine and outcome data. Since trajectory data are collected at a higher frequency (1000 Hz) with respect to image data (200 Hz), the former are sub-sampled, to bring all measurements on a common clock. The last step is therefore:

(c) **Registration of machine time history and process feedback.**

A laser activation signal is estimated from the melt pool images, labeling as *laser ON* images the ones with mean pixel intensity greater than a background noise threshold. The true *laser ON* signal, available within machine data, is registered to the image-estimated activation signal by minimization of the cross-correlation, thus allowing to establish for both a shared timestamp.

The resulting data set includes the following variables, all recorded at a common clock of 200 Hz:

- timestamp;
- laser spot velocity modulus  $V$  (computed from the original trajectory at 1 kHz sampling rate);
- emitted laser power  $P$ ;
- filename of corresponding image;
- *laser ON* binary signal;
- process outcomes  $H$ ,  $W$  and  $A$ .

Moreover, the following, derived boolean features, depicted in Fig. 7, have been added:

- *accelerating*, set to one when  $V$  is increasing;
- *decelerating*, set to one when  $V$  is decreasing;
- *stable*, set to one when  $V$  is constant;

they are set to zero otherwise. These features have been introduced to account for the differences observed in the deposited tracks outside a stationary regime.

Finally, the following image features have been computed and added to the integrated data set to train a simpler linear model, that used is Section 4 to demonstrate the advantages offered by the DLS approach:

- mean image intensity  $I_{\text{mean}}$  and its moving average on 10 timestamps  $I_{\text{movemean}}$
- mean image intensity on a cropped subregion of  $200 \times 200$  pixels  $I_{\text{Cmean}}$  and its moving average on 10 timestamps  $I_{\text{Cmovemean}}$

### 3.3. Deep-learning system design

A deep-learning system has been designed to predict the track geometries in terms of width, height and cross-section. The DLS needs to account for image as well as numerical data inputs. The DLS achieves this by stacking two neural networks, i.e. a convolutional one and a *combined network*, as depicted in Fig. 8, similarly to [30]. CNNs are the go-to approach for computer vision tasks, achieving state-of-the-art performance, such as [37], by using multiple filters sliding over the image and detecting certain patterns and spatial context. The convolutional part is fed with the image resized as a tensor with dimensions (224, 224, 3), being the output of a standard preprocessing pipeline for CNNs [38], which is then processed by convolutional layers and the subsequent fully connected dense layers. The consecutive combined part is a standard dense neural network, which receives as input from the convolutional part a vector of varying size (depending on the chosen architecture), joint with the numerical input data ( $P, V$ ) as well as the one-hot-encoded phases (accelerating, decelerating and stable), and as outputs the process outcomes  $W$ ,  $H$  and  $A$ .

For the convolutional part, in each block traditional max-pooling layers have been replaced by additional convolutional layers with stride 3, as suggested in [39]. Dropout with probability 0.2 has been consistently applied after each block, except the first one. Transfer learning, i.e. the use of pre-trained nets, could not be employed, since most readily available CNNs have been mainly trained on images in a scenic setting, which have little in common with the present use case, as preliminary results suggest. The subsequent combined neural

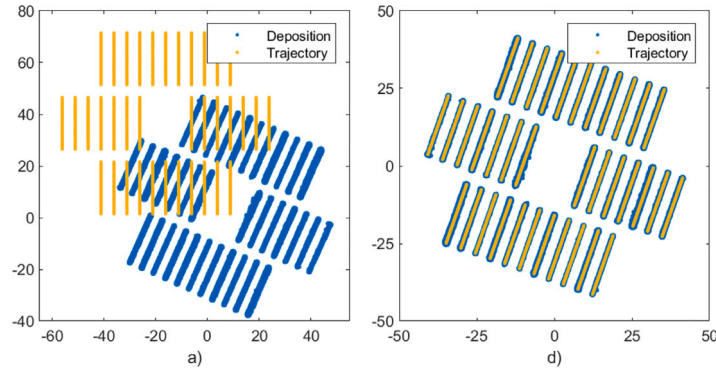


Fig. 5. (a) Initial and (b) final state of geometry alignment step.

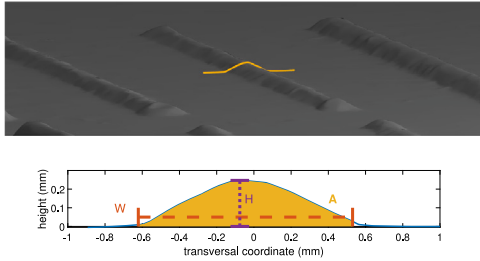


Fig. 6. Top panel: detail of 3D-scanned surface, with superimposed profile of a cross-section. Bottom panel: cross-section profile and outcome measurements ( $W$ ,  $H$  and  $A$ ).

Table 1

Hyperparameters values used for the deep-learning system. The number of layers is indicated by the length of the vector, whereas the explicit number refers to (i) the number of filters applied in case of convolutional layers, or (ii) the number of neurons in case of standard neural networks. All possible combinations were employed for training and testing.

| Hyperparameter       | Values  |
|----------------------|---|
| Convolutional layers | [16, 32, 64, 128], [16, 16, 32, 32], [16, 32, 64], [32, 32, 32], [16, 64] |
| Kernel sizes         | 2, 3  |
| Dense layers         | [256, 128], [64, 32], [16, 3]   |
| Combined             | [512, 16], [128, 16], [32, 16]  |

network concatenates the resulting vector of the CNN with numerical and one-hot encoded data, and finally outputs the required targets. A full overview of the hyperparameters used during training can be found in Table 1. The DLS technically consists of two neural networks, the convolutional and combined part, whereas training occurs end-to-end, meaning that from a backpropagation perspective the two networks have been treated as unified. RMSprop [40] has been used as optimizer. Only data relative to deposited tracks (i.e. with laser signal ON) have been employed for training and testing the system.

The results of the DLS have been compared against a linear regression model used as a baseline. The linear baseline (LBL) does not take into account the deposition images, but employs the image brightness ( $I_{\text{mean}}$ ,  $I_{\text{Cmean}}$ ,  $I_{\text{movemean}}$  or  $I_{\text{Cmovemean}}$ ), the nominal power, the deposition speed and three additional one-hot-encoded phases as input. A different linear model has been trained for each brightness input.

The deposition data have been split for training and testing the DLS against the LBL. The same splits have been used for both systems. All data points coming from a single track have been assigned either to the training or the test set. The available 36 tracks have been split into 4 random folds and used for training and testing using a cross-validation strategy [41], repeated 5 times. The input features have been scaled to have zero mean and unit variance.

The models have been evaluated and compared in terms of Mean Squared Error (MSE) defined as:

$$MSE(y, \hat{f}(x)) = \frac{1}{np} \sum_{i=1}^n \sum_{j=1}^p (y_{ij} - \hat{f}_j(x_i))^2 \quad (1)$$

where  $\hat{f}_j(x_i)$  is the model prediction of the  $j$ th output for the  $i$ th data point and  $y_{ij}$  is the corresponding target value [41]. For the proposed model, which includes three process outcomes ( $W$ ,  $H$  and  $A$ ),  $p = 3$ .

The training and testing have been performed on a system comprising two Intel Xeon Silver 4114 CPUs and four NVIDIA RTX2080TI GPUs. On this system, one training epoch lasts 6–15 s and the training of one model for 30 epochs lasts between 250–360 s. The prediction of the geometry for one specific data point (i.e. one image and the relative numerical input data and one-hot-encoded phases), including preprocessing, lasts 38 ms.

#### 4. Experimental results

The data collected during the experimental campaign (Section 3.1) have been treated with the proposed data fusion pipeline (Section 3.2), thus creating the integrated data set used for testing the described DLS approach. Such dataset is available at [42].

The DLS has been trained and tested using the hyperparameters and cross-validation strategy described in Section 3.3. The effects of the hyperparameters on the performance are depicted in Fig. 9, where each box plot represents the distribution of the MSE for different DLS architectures. Fig. 9a shows that the architectures with just two convolutional layers exhibit higher mean squared errors with respect to systems having three or four convolutional layers. The number of filters in each layer does not appear to have a significant effect. The higher values of MSE observed for the kernel sizes [2, 2] and [3, 3] (Fig. 9d) can also be attributed to the presence of just two convolutional layers. No significant effect on the performance of the system are observed varying the size of the fully connected layers (Fig. 9a and b). The DLS already shows very good performances with a small amount of neurons for the combined network, resulting in reduced training times and risk of overfitting.

The DLS shows better performance when compared with the LBL. Fig. 10 depicts the predictions of the LBL (green circles) and of the DLS (blue crosses) versus the real values of process outcomes  $W$ ,  $H$  and  $A$ . The dashed line represents an ideal prediction with zero error (i.e.  $y_{ij} = \hat{f}_j(x_i)$ ). The data points reported in Fig. 10 are relative to three representative test tracks relative to the deposition parameters (600 W, 1050 mm/min), (700 W, 300 mm/min) and (300 W, 450 mm/min). All points of these tracks have never been seen from the models during training. No significant difference between the DLS and the LBL can be observed for the predictions of the track width for these tracks (Fig. 10a), whereas the LBL shows a bigger bias in the prediction of the track height and cross-section area, respectively, as clusters of

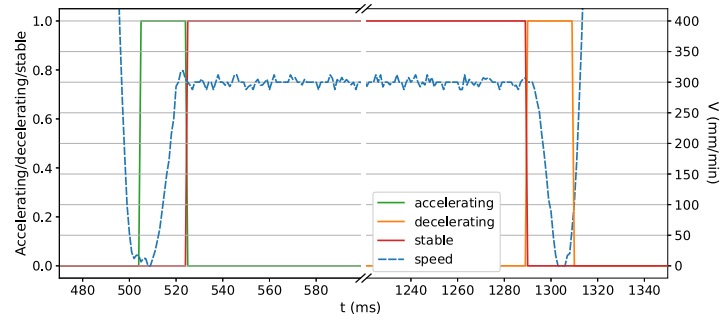


Fig. 7. Boolean features *accelerating*, *decelerating* and *stable* (left-side axis) and deposition speed (right-side axis) as a function of deposition time.

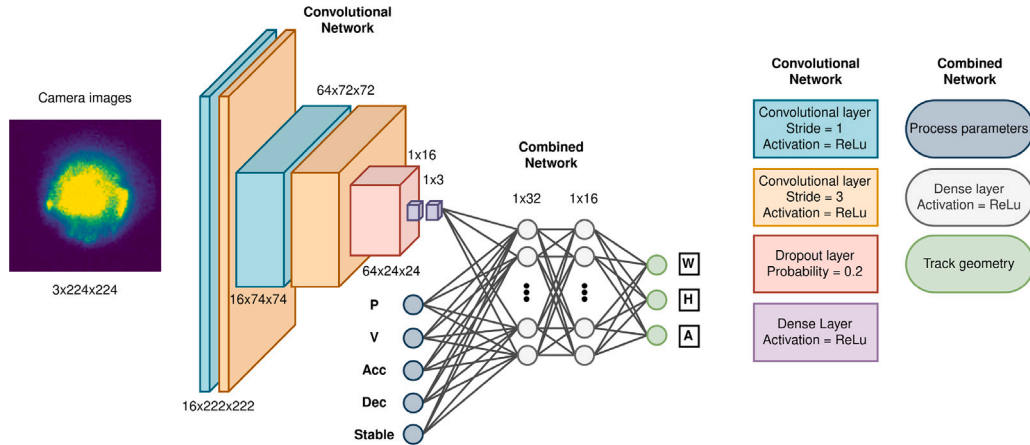


Fig. 8. Deep-learning system architecture. First, a CNN is applied to the image tensor, and subsequently a neural network is applied to the output of the CNN concatenated with  $P$ ,  $V$  and the one-hot-encoded three phases (accelerating, stable, decelerating). Max-Pooling has been replaced with another convolutional layer with stride 3, such that each convolutional block contains two convolutional layers. In this example, the CNN outputs a vector of size three, which is then concatenated with the numerical data input to a vector of size eight.

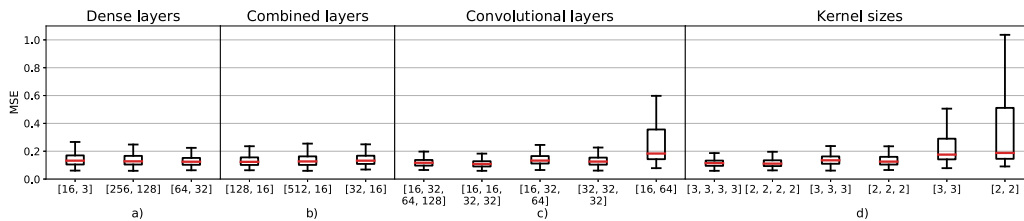


Fig. 9. Mean squared error distribution for different DLS architectures. The red solid lines represent the median values of the MSE distributions for the different hyperparameters. For each box plot, the parameter indicated on the  $x$ -axis is fixed and all the possible combinations of the other hyperparameters are reported. (For interpretation of the references to color in this figure legend, the reader is referred to the web version of this article.)

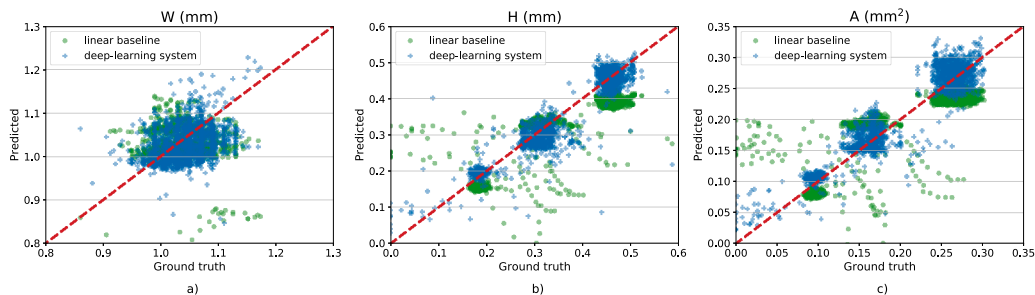
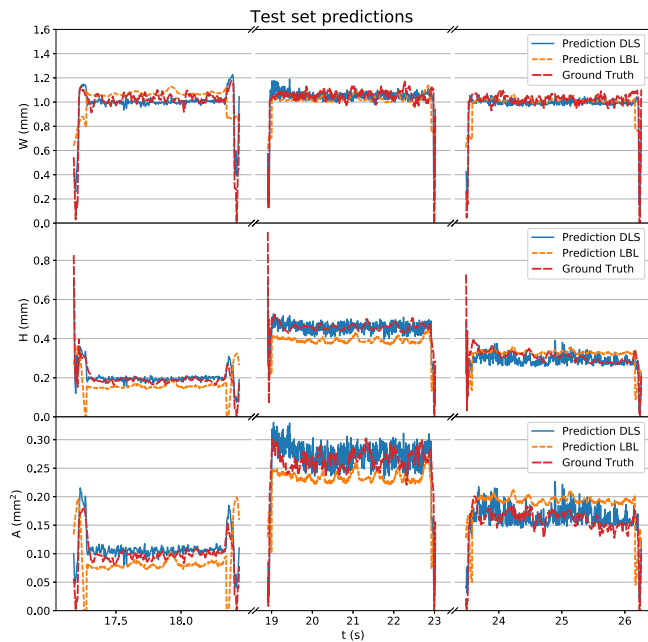
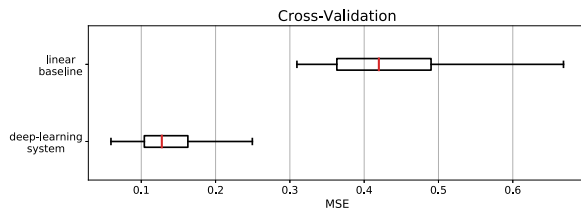


Fig. 10. Deep-learning system (green circles) and linear baseline (blue crosses) predictions versus real track geometry values (ground truth) for three representative test tracks. The dashed line represents an ideal prediction with zero error. The tracks have been deposited with the following parameters: (600 W, 1050 mm/min), (700 W, 300 mm/min), (300 W, 450 mm/min).



**Fig. 11.** Deep-learning system and linear baseline predictions for the track geometry (ground truth) as a function of the deposition time for three representative test tracks. The tracks have been deposited with the following parameters: (600 W, 1050 mm/min), (700 W, 300 mm/min), (300 W, 450 mm/min).



**Fig. 12.** Deep-learning system and linear baseline MSE distribution. For the deep-learning system, all hyperparameters combinations as well as all CV-folds have been represented (1800 models in total). For the linear baseline, all predictors as well as all CV-folds are reported (80 models in total).

prediction points at a bigger distance from the  $y_{ij} = \hat{f}_j(x_i)$  line are present in Fig. 10b and c. The same effect can be observed in Fig. 11, where the predicted values for the DLS and for the LBL are shown as a function of the deposition time for the same tracks. The ground truth, i.e. the real values of the track geometries, are depicted by the red dashed lines. Fig. 11 not only underlines the higher performance of the DLS in predicting the average values of the track geometry, i.e. the lower prediction bias, but it also shows that the DLS has a better capability in following the evolution of  $W$ ,  $H$  and  $A$  during the transients at the beginning and ending of the track, i.e. where the deposition speed is not constant. As such transients are much more present when depositing more complex parts with AM, the better prediction capability of the DLS in these conditions makes it a very good candidate for predicting more complex geometries. An accurate prediction of the geometry during transients is also a prerequisite for on-line process control, with the potential to reduce the dimension deviations of the deposited parts and therefore their subsequent post-processing.

Fig. 12 depicts a quantitative comparison between the LBL and the DLS in terms of MSE and it clearly indicates that the latter has superior predicting capabilities. The boxplots represent the MSE distribution for all the hyperparameters combinations and cross-validation folds (DLS, 1800 points in total), and for all the brightness features and cross-validation folds (LBL, 80 points in total). The better performance of the DLS can be explained by the fact that the DLS is indeed able

to take advantage of the deposition images as a whole and not only of its average intensity, as it is the case for the LBL. The images can contain additional information (such as the melt pool shape or the presence of sparks) which are relevant for the prediction of the track geometry (Fig. 2). An additional advantage of using a system containing CNNs is that all these information are modeled without the need of explicitly coding them into features. This is a promising starting point for extending the system to more complicated settings, such as complex geometries and on-line process control, where hard-coded features would need to be adapted or newly defined. Moreover, such a system can also be newly trained using data coming from the deposition of different materials, allowing for a deployment for a wide range of applications.

## 5. Conclusions

The proposed approach allows to predict geometric outcomes of a LMD process with a good degree of accuracy, compared to other machine learning methods suitable for on-line prediction in this context. Moreover, the data acquisition and processing pipeline could be applied on nearly any LMD machine, as it exploits signals that are usually readily available or easily integrable on such equipment. The proposed DLS allows to effectively extract information from melt pool images, also thanks to the particular network design that blends image and scalar variables within the last layers of the deep structure, providing a starting point for experimenting with deeper and more sophisticated network structures. In fact, the results demonstrate that the proposed DLS is far more performing than a linear baseline, with the additional advantage that image filters learned by the CNN layers must not be hard-coded, in contrast with traditional image processing methods, which to present day had few success in determining significant image features *a priori*.

The obtained results indicate that the proposed methodology is promising for being applied to more general cases, for example to generic geometries and different materials. In these cases, the model will be revised with new training data and updated hyperparameters, to capture new, more complex process dynamics; nonetheless, the approach should still hold, in particular by leveraging the transfer learning capability of CNNs, i.e., networks that have been trained for another related task can often be adjusted to be used successfully on a different application by re-training some of the weights. For example, a system trained on single tracks could be extended to predict more complex 2-D geometries.

Moreover, the same framework could be applied in the future with additional variables as either outputs (e.g. porosity, measured from sample cuts) or inputs (e.g. melt pool temperature from a pyrometer). In particular, training extended models that use layer index as additional input variable will constitute an important challenge when dealing with thick geometries, as track height cannot be easily measured for intermediate deposition layers.

Finally, the proposed approach could be used as the basis for a model predictive process controller, which is a key enabler for improving the quality of LMD parts in general cases.

## CRedit authorship contribution statement

**Martina Perani:** Conceptualization, Methodology, Software, Validation, Formal analysis, Writing – original draft, Writing – review & editing, Visualization. **Stefano Baraldo:** Conceptualization, Methodology, Software, Validation, Investigation, Writing – original draft, Writing – review & editing, Visualization, Project administration. **Michael Decker:** Software, Validation. **Ambra Vandone:** Conceptualization, Methodology, Software. **Anna Valente:** Supervision, Funding acquisition. **Beatrice Paoli:** Supervision, Funding acquisition.

## Declaration of competing interest

No author associated with this paper has disclosed any potential or pertinent conflicts which may be perceived to have impending conflict with this work. For full disclosure statements refer to <https://doi.org/10.1016/j.rcim.2022.102445>.

## Data availability

The reference to on-line available data is present in the manuscript.

## Acknowledgment

This work was supported in part by SUPSI-FFHS, Switzerland internal project DED-In718 and by the Swiss National Science Foundation (SNSF) project *Ground Control* (grant number 179014).

## References

- [1] M. Schmidt, M. Merklein, D. Bourell, D. Dimitrov, T. Hausotte, K. Wegener, L. Overmeyer, F. Vollertsen, G.N. Levy, Laser based additive manufacturing in industry and academia, *CIRP Ann.* 66 (2) (2017) 561–583, URL <https://www.sciencedirect.com/science/article/pii/S0007850617301506>.
- [2] Z.U. Arif, M.Y. Khalid, A.A. Rashid, E. ur Rehman, M. Atif, Laser deposition of high-entropy alloys: A comprehensive review, *Opt. Laser Technol.* 145 (2022).
- [3] S. Wang, L. Zhu, J.Y.H. Fuh, H. Zhang, W. Yan, Multi-physics modeling and Gaussian process regression analysis of cladding track geometry for direct energy deposition, *Opt. Lasers Eng.* 127 (September 2019) (2020).
- [4] J.I. Arrizubieta, A. Lamikiz, F. Klocke, S. Martínez, K. Arntz, E. Ukar, Evaluation of the relevance of melt pool dynamics in laser material deposition process modeling, *Int. J. Heat Mass Transfer* 115 (2017) 80–91.
- [5] D. Kono, H. Yamaguchi, Y. Oda, T. Sakai, Stabilization of standoff distance by efficient and adaptive updating of layer height command in directed energy deposition, *CIRP J. Manuf. Sci. Technol.* 31 (2020) 244–250.
- [6] O. Avram, C. Fellows, M. Menerini, A. Valente, Automated platform for consistent part realization with regenerative hybrid additive manufacturing workflow, *Int. J. Adv. Manuf. Technol.* 119 (3–4) (2022) 1737–1755.
- [7] A.R. Nassar, J.S. Keist, E.W. Reutzel, T.J. Spurgeon, Intra-layer closed-loop control of build plan during directed energy additive manufacturing of Ti-6Al-4V, *Addit. Manuf.* 6 (2015) 39–52, URL <http://dx.doi.org/10.1016/j.addma.2015.03.005>.
- [8] A. Vandone, S. Baraldo, A. Valente, F. Mazzucato, Vision-based melt pool monitoring system setup for additive manufacturing, *Procedia CIRP* 81 (2019) 747–752, URL <https://www.sciencedirect.com/science/article/pii/S2212827119304937>.
- [9] M.H. Farshidianfar, F. Khodabakhshi, A. Khajepour, A.P. Gerlich, Closed-loop control of microstructure and mechanical properties in additive manufacturing by directed energy deposition, *Mater. Sci. Eng. A* 803 (2021) 140483.
- [10] T. Staudt, E. Eschner, M. Schmidt, Temperature determination in laser welding based upon a hyperspectral imaging technique, *CIRP Ann.* 68 (1) (2019) 225–228.
- [11] C. Prieto, R. Fernandez, C. Gonzalez, M. Diez, J. Arias, R. Sommerhuber, F. Lücking, In situ process monitoring by optical microphone for crack detection in laser metal deposition applications, in: 11 Th CIRP Conference on Photonic Technologies, Lane 2020, 2020.
- [12] T. Purtonen, A. Kalliosaari, A. Salminen, Monitoring and adaptive control of laser processes, *Physics Procedia* 56 (C) (2014) 1218–1231.
- [13] N. Shamsaei, A. Yadollahi, L. Bian, S.M. Thompson, An overview of direct laser deposition for additive manufacturing; Part II: Mechanical behavior, process parameter optimization and control, *Addit. Manuf.* 8 (2015) 36–62, URL <https://www.sciencedirect.com/science/article/pii/S2214860415000329>.
- [14] M.A. Naiel, D.S. Ertay, M. Vlasea, P. Fieguth, Adaptive vision-based detection of laser-material interaction for directed energy deposition, *Addit. Manuf.* 36 (June) (2020) 101468.
- [15] Z. Zhang, Z. Liu, D. Wu, Prediction of melt pool temperature in directed energy deposition using machine learning, *Addit. Manuf.* 37 (November 2020) (2021) 101692.
- [16] R. Leach, D. Bourell, S. Carmignato, A. Donmez, N. Senin, W. Dewulf, Geometrical metrology for metal additive manufacturing, *CIRP Ann.* 68 (2) (2019) 677–700, URL <https://www.sciencedirect.com/science/article/pii/S0007850619301611>.
- [17] P.I. Stavroulakis, R.K. Leach, Invited review article: Review of post-process optical form metrology for industrial-grade metal additive manufactured parts, *Rev. Sci. Instrum.* 87 (4) (2016).
- [18] A. Thompson, I. Maskery, R.K. Leach, X-ray computed tomography for additive manufacturing: A review, *Meas. Sci. Technol.* 27 (2016) 072001.
- [19] X. Qi, G. Chen, Y. Li, X. Cheng, C. Li, Applying neural-network-based machine learning to additive manufacturing: Current applications, challenges, and future perspectives, *Engineering* 5 (4) (2019) 721–729, URL <http://www.sciencedirect.com/science/article/pii/S2095809918307732>.
- [20] A. Equbal, A.K. Sood, S. Mahapatra, Prediction of dimensional accuracy in fused deposition modelling: A fuzzy logic approach, *Int. J. Product. Qual. Manage.* 7 (1) (2011) 22–43.
- [21] S.L. Sing, C.N. Kuo, C.T. Shih, C.C. Ho, C.K. Chua, Perspectives of using machine learning in laser powder bed fusion for metal additive manufacturing, *Virtual Phys. Prototyp.* 16 (2021) 372–386.
- [22] A.K. Sood, R.K. Ohdar, S.S. Mahapatra, Parametric appraisal of mechanical property of fused deposition modelling processed parts, *Mater. Des.* 31 (1) (2010) 287–295.
- [23] X. Shen, J. Yao, Y. Wang, J. Yang, Density prediction of selective laser sintering parts based on artificial neural network, in: *International Symposium on Neural Networks*, Springer, 2004, pp. 832–840.
- [24] X.-f. Li, J.-h. Dong, Y.-z. Zhang, Modeling and applying of RBF neural network based on fuzzy clustering and pseudo-inverse method, in: *2009 International Conference on Information Engineering and Computer Science*, IEEE, 2009, pp. 1–4.
- [25] J. Munguia, J. Ciurana, C. Riba, Neural-network-based model for build-time estimation in selective laser sintering, *Proc. Inst. Mech. Eng. B* 223 (8) (2009) 995–1003.
- [26] W. Rong-Ji, L. Xin-Hua, W. Qing-Ding, W. Lingling, Optimizing process parameters for selective laser sintering based on neural network and genetic algorithm, *Int. J. Adv. Manuf. Technol.* 42 (11–12) (2009) 1035–1042.
- [27] A. Garg, K. Tai, M. Savalani, State-of-the-art in empirical modelling of rapid prototyping processes, *Rapid Prototyp. J.* (2014).
- [28] R.-J. Wang, J. Li, F. Wang, X. Li, Q. Wu, ANN model for the prediction of density in selective laser sintering, *Int. J. Manuf. Res.* 4 (3) (2009) 362–373.
- [29] F. Caiazzo, A. Caggiano, Laser direct metal deposition of 2024 Al alloy: Trace geometry prediction via machine learning, *Materials* 11 (3) (2018) 444.
- [30] J. Francis, L. Bian, Deep learning for distortion prediction in laser-based additive manufacturing using big data, *Manuf. Lett.* 20 (2019) 10–14, URL <http://www.sciencedirect.com/science/article/pii/S221384631830172X>.
- [31] M. Khanzadeh, S. Chowdhury, M. Marufuzzaman, M.A. Tschopp, L. Bian, Porosity prediction: Supervised-learning of thermal history for direct laser deposition, *J. Manuf. Syst.* 47 (2018) 69–82, URL <http://www.sciencedirect.com/science/article/pii/S0278612518300402>.
- [32] J. Zhang, P. Wang, R.X. Gao, Deep learning-based tensile strength prediction in fused deposition modeling, *Comput. Ind.* 107 (2019) 11–21, URL <http://www.sciencedirect.com/science/article/pii/S0166361518305815>.
- [33] F. Mazzucato, D. Forni, A. Valente, E. Cadoni, Laser metal deposition of Inconel 718 alloy and as-built mechanical properties compared to casting, *Metals* 14 (437) (2021) 1–21.
- [34] A. Vandone, S. Baraldo, A. Valente, Multisensor data fusion for additive manufacturing process control, *IEEE Robot. Autom. Lett.* 3 (4) (2018) 3279–3284, URL <https://ieeexplore.ieee.org/document/8400414/>.
- [35] T. Hastie, R. Tibshirani, J. Friedman, *The Elements of Statistical Learning*, second ed., Springer, New York, 2009, URL [http://statweb.stanford.edu/~tibs/book/preface.ps](http://statweb.stanford.edu/~tibs/book/preface.ps%0Ahttp://www-stat.stanford.edu/~tibs/book/preface.ps).
- [36] P. Besl, N. McKay, A method for registration of 3-D shapes, *IEEE Trans. Pattern Anal. Mach. Intell.* 14 (2) (1992) 239–256.
- [37] A. Krizhevsky, I. Sutskever, G.E. Hinton, Imagenet classification with deep convolutional neural networks, in: *Advances in Neural Information Processing Systems*, 2012, pp. 1097–1105.
- [38] K. Simonyan, A. Zisserman, Very deep convolutional networks for large-scale image recognition, in: Y. Bengio, Y. LeCun (Eds.), *3rd International Conference on Learning Representations, ICLR 2015*, San Diego, CA, USA, May 7–9, 2015, Conference Track Proceedings, 2015, URL <http://arxiv.org/abs/1409.1556>.
- [39] J.T. Springenberg, A. Dosovitskiy, T. Brox, M. Riedmiller, Striving for simplicity: The all convolutional net, 2015, [cs.LG] [arXiv:1412.6806](https://arxiv.org/abs/1412.6806), URL <https://arxiv.org/abs/1412.6806>.
- [40] G. Hinton, N. Srivastava, K. Swersky, Neural networks for machine learning, lecture 6., 2012, URL <http://www.cs.toronto.edu/~hinton/coursera/lecture6/lec6.pdf>.
- [41] G. James, D. Witten, T. Hastie, R. Tibshirani, *An Introduction to Statistical Learning with Applications in R*, second ed., Springer, 2021, URL <https://www.statlearning.com/>.
- [42] S. Baraldo, LMD inconel 718 single tracks, 2020, Zenodo URL <https://doi.org/10.5281/zenodo.3978982>.